Fiber-optic and articulating arm implementations of laminar optical tomography for clinical applications

Sean A. Burgess,[1,*] Désirée Ratner,[2] Brenda R. Chen,[1] and Elizabeth M. C. Hillman[1]

[1]*Laboratory for Functional Optical Imaging, Departments of Biomedical Engineering and Radiology, Columbia University, New York, NY 10027, USA*

[2]*Department of Dermatology, Columbia University Medical Center, New York, NY 10027, USA*

**sab2161@columbia.edu*

Abstract: Laminar optical tomography (LOT) is a recently developed technique for depth-resolved *in vivo* imaging of absorption and fluorescence contrast. Until now, LOT has been implemented in a benchtop configuration, limiting accessibility to tissues and restricting imaging applications. Here we report on LOT implemented through an articulating arm and a fiber optic image bundle allowing flexible imaging for a range of clinical applications. We quantify the performance of these two implementations by imaging a tissue mimicking phantom.

OCIS codes: (170.3880) Medical and biological imaging; (170.3890) Medical optics instrumentation

References and links

1. J. de Leeuw, N. van der Beek, W. D. Neugebauer, P. Bjerring, and H. A. Neumann, "Fluorescence detection and diagnosis of non-melanoma skin cancer at an early stage," Lasers Surg. Med. **41**(2), 96–103 (2009).
2. B. Stenquist, M. B. Ericson, C. Strandeberg, L. Mölne, A. Rosén, O. Larkö, and A. M. Wennberg, "Bispectral fluorescence imaging of aggressive basal cell carcinoma combined with histopathological mapping: a preliminary study indicating a possible adjunct to Mohs micrographic surgery," Br. J. Dermatol. **154**(2), 305–309 (2006).
3. R. Kiesslich, J. Burg, M. Vieth, J. Gnaendiger, M. Enders, P. Delaney, A. Polglase, W. McLaren, D. Janell, S. Thomas, B. Nafe, P. R. Galle, and M. F. Neurath, "Confocal laser endoscopy for diagnosing intraepithelial neoplasias and colorectal cancer in vivo," Gastroenterology **127**(3), 706–713 (2004).
4. K. B. Dunbar, P. Okolo 3rd, E. Montgomery, and M. I. Canto, "Confocal laser endomicroscopy in Barrett's esophagus and endoscopically inapparent Barrett's neoplasia: a prospective, randomized, double-blind, controlled, crossover trial," Gastrointest. Endosc. **70**(4), 645–654 (2009).
5. R. Kiesslich, L. Gossner, M. Goetz, A. Dahlmann, M. Vieth, M. Stolte, A. Hoffman, M. Jung, B. Nafe, P. R. Galle, and M. F. Neurath, "In vivo histology of Barrett's esophagus and associated neoplasia by confocal laser endomicroscopy," Clin. Gastroenterol. Hepatol. **4**(8), 979–987 (2006).
6. B. R. Haxel, M. Goetz, R. Kiesslich, and J. Gosepath, "Confocal endomicroscopy: a novel application for imaging of oral and oropharyngeal mucosa in human," Eur. Arch. Otorhinolaryngol. **267**(3), 443–448 (2010).
7. R. A. Schwarz, W. Gao, C. Redden Weber, C. Kurachi, J. J. Lee, A. K. El-Naggar, R. Richards-Kortum, and A. M. Gillenwater, "Noninvasive evaluation of oral lesions using depth-sensitive optical spectroscopy," Cancer **115**(8), 1669–1679 (2009).
8. J. Tan, M. A. Quinn, J. M. Pyman, P. M. Delaney, and W. J. McLaren, "Detection of cervical intraepithelial neoplasia in vivo using confocal endomicroscopy," BJOG **116**(12), 1663–1670 (2009).
9. M. Rajadhyaksha, R. R. Anderson, and R. H. Webb, "Video-rate confocal scanning laser microscope for imaging human tissues in vivo," Appl. Opt. **38**(10), 2105–2115 (1999).
10. E. M. C. Hillman, O. Bernus, E. Pease, M. B. Bouchard, and A. Pertsov, "Depth-resolved optical imaging of transmural electrical propagation in perfused heart," Opt. Express **15**(26), 17827–17841 (2007).
11. E. M. C. Hillman, D. A. Boas, A. M. Dale, and A. K. Dunn, "Laminar optical tomography: demonstration of millimeter-scale depth-resolved imaging in turbid media," Opt. Lett. **29**(14), 1650–1652 (2004).
12. S. A. Burgess, M. B. Bouchard, B. Yuan, and E. M. C. Hillman, "Simultaneous multiwavelength laminar optical tomography," Opt. Lett. **33**(22), 2710–2712 (2008).
13. N. Ouakli, E. Guevara, S. Dubeau, É. Beaumont, and F. Lesage, "Laminar optical tomography of the hemodynamic response in the lumbar spinal cord of rats," Opt. Express **18**(10), 10068–10077 (2010).
14. S. Yuan, Q. Li, J. Jiang, A. Cable, and Y. Chen, "Three-dimensional coregistered optical coherence tomography and line-scanning fluorescence laminar optical tomography," Opt. Lett. **34**(11), 1615–1617 (2009).
15. E. M. C. Hillman, "Optical brain imaging in vivo: techniques and applications from animal to man," J. Biomed. Opt. **12**(5), 051402 (2007).

#129559 - $15.00 USD Received 4 Jun 2010; revised 28 Aug 2010; accepted 31 Aug 2010; published 2 Sep 2010

16. P. M. Lane, S. Lam, A. McWilliams, J. C. Leriche, M. W. Anderson, and C. E. Macaulay, "Confocal fluorescence microendoscopy of bronchial epithelium," J. Biomed. Opt. **14**(2), 024008 (2009).
17. K. B. Sung, R. Richards-Kortum, M. Follen, A. Malpica, C. Liang, and M. Descour, "Fiber optic confocal reflectance microscopy: a new real-time technique to view nuclear morphology in cervical squamous epithelium in vivo," Opt. Express **11**(24), 3171–3181 (2003).
18. B. Yuan, S. A. Burgess, A. Iranmahboob, M. B. Bouchard, N. Lehrer, C. Bordier, and E. M. C. Hillman, "A system for high-resolution depth-resolved optical imaging of fluorescence and absorption contrast," Rev. Sci. Instrum. **80**(4), 043706 (2009).
19. F. C. Allard, *Fiber optics handbook: for engineers and scientists*, Optical and electro-optical engineering series (McGraw-Hill, New York, 1990), p. 549 p. in various pagings.
20. R. Cubeddu, A. Pifferi, P. Taroni, A. Torricelli, and G. Valentini, "A solid tissue phantom for photon migration studies," Phys. Med. Biol. **42**(10), 1971–1979 (1997).
21. M. Lualdi, A. Colombo, M. Carrara, L. Scienza, S. Tomatis, and R. Marchesini, "Optical devices used for image analysis of pigmented skin lesions: a proposal for quality assurance protocol using tissue-like phantoms," Phys. Med. Biol. **51**(23), N429–N440 (2006).
22. E. M. C. Hillman, and S. A. Burgess, "Sub-millimeter resolution 3D optical imaging of living tissue using laminar optical tomography," Laser Photon Rev **3**(1-2), 159–179 (2009).
23. K. B. Sung, C. Liang, M. Descour, T. Collier, M. Follen, and R. Richards-Kortum, "Fiber-optic confocal reflectance microscope with miniature objective for in vivo imaging of human tissues," IEEE Trans. Biomed. Eng. **49**(10), 1168–1172 (2002).
24. R. Juškattis, T. Wilson, and T. F. Watson, "Real-time white light reflection confocal microscopy using a fibre-optic bundle," Scanning **19**(1), 15–19 (1997).

1. Introduction

Optical imaging of superficial tissues has the potential to find widespread use in medical diagnostics, surgical guidance, and in situ monitoring. Blood volume and oxygenation, two important biological parameters, can be characterized through optical measurements at different wavelengths. Fluorescence measurements, either from autofluorescence or fluorescent dyes, have shown promise for helping to identify and analyze lesions in various epithelial tissues including skin [1,2], colon [3], esophagus [4,5], oral mucosa [6,7], and cervix [8].

The optical sectioning capability of confocal microscopy has made it a promising technology for imaging such tissues with microscopic resolution at depths of up to a few hundred microns within tissue. However, while capable of resolving cell morphology and tissue architecture, confocal microscopy has limited utility for deeper tissues [9]. Further, when operated in reflectance mode, contrast is primarily governed by the amount of back-scattering rather than absorption. In fact, in both fluorescence and reflectance modes the absorption properties of a specimen have a negative impact on image contrast by attenuating the illuminated beam and backscattered or fluorescence signal. As a result, confocal microscopy is not used to image absorption contrast such as that provided by hemoglobin and melanin.

Laminar optical tomography (LOT) is a recently developed technique for imaging absorption and fluorescence contrast to depths of up to 2 mm in biological tissue [10,11]. Simultaneous collection of off-axis remitted light at multiple narrow source-detector separations enables rapid acquisition of depth-sensitive measurements. Such measurements bridge the gap between confocal microscopy and diffuse optical tomography, providing penetration depths beyond those of confocal microscopy with resolution exceeding that of diffuse optical techniques. Like confocal microscopy, LOT can image fluorescence contrast but has the added benefit of imaging absorption contrast as well. Previous LOT systems reported by us [11,12] and other groups [13,14] have been implemented in a rigid benchtop configuration. While initially developed for in-vivo imaging of the rodent brain [15], potential applications of LOT extend beyond the confines of a benchtop setup to include clinical targets for which accessibility becomes a challenge. Fluorescence [3,16] and reflectance [9,17] confocal microscopy have been miniaturized to facilitate clinical imaging. In order to translate LOT to clinical applications and reach otherwise inaccessible regions of the body, a more flexible patient interface becomes necessary.

Here, we present two LOT configurations to facilitate clinical imaging: LOT implemented with an articulating arm and LOT implemented through a flexible fiber bundle. We used our

#129559 - $15.00 USD Received 4 Jun 2010; revised 28 Aug 2010; accepted 31 Aug 2010; published 2 Sep 2010

newly developed interfaces to image a phantom demonstrating the ability of each configuration to acquire LOT data.

2. System design

This section describes the implementation of the new LOT interfaces. In the first part, a description of LOT's measurement geometry is provided along with a basic system layout. We then describe how the system was modified to incorporate the articulating arm and fiber bundle and discuss the challenges associated with each.

2.1 Laminar optical tomography

Figure 1(a) shows a schematic of LOT's measurement geometry. Light enters the tissue at a source position (s_1), while light emerging at several, relatively short, distances (typically 0 to 3 mm away) from the source position (d_1 to d_7) is simultaneously detected. Collection of this off-axis remitted light facilitates depth discrimination since light emitting further from the source position has, on average, scattered more deeply into the tissue [Fig. 1(a)]. To obtain an image of a sample, a two-dimensional scan of the source position is performed resulting in a p_x x p_y x d LOT data set where p_x and p_y are the number of pixels in the x and y directions respectively and d is the number of off-axis detectors.

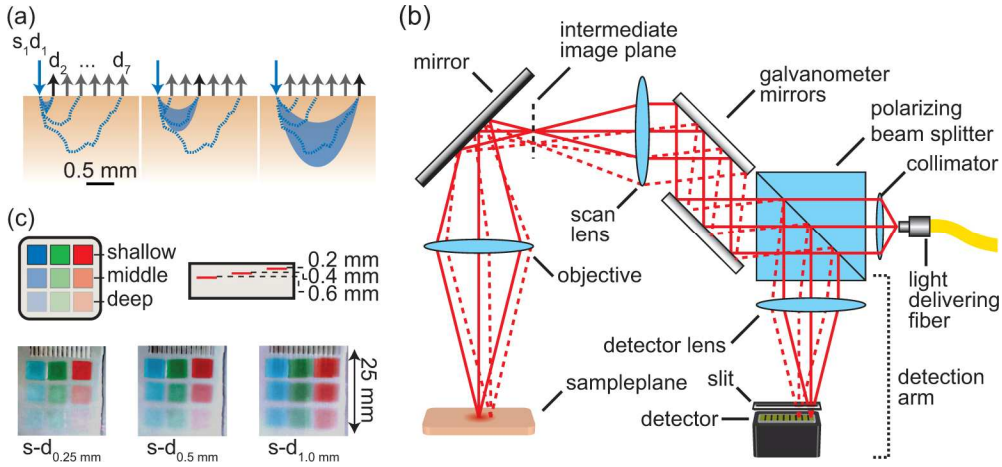

Fig. 1. (a) Schematic showing remitted reflected light paths within tissue. Light emitted further from the source has, on average, travelled deeper into the tissue. (b) Schematic of basic LOT system for absorption contrast imaging. (c) RGB merged raw LOT data of a phantom with red, green and blue absorbers embedded at different depths. The narrow source-detector separation (0.25 mm) is more sensitive to shallow embedded absorbers. In the wider source-detector separation (1.0 mm) the deeper embedded absorbers become more apparent.

The basic design of an LOT system is similar to that of a confocal laser scanning microscope and is shown in Fig. 1(b). A polarization maintaining fiber delivers linearly polarized light that passes through a polarizing beam splitter cube before being scanned by a set of galvanometer mirrors and focused onto the surface of a sample. Light undergoes absorption and scattering events within the sample reducing its intensity and randomizing its polarization state. On-axis light emitting from the sample travels back along the same path as the incident light towards the galvanometer mirrors, where it's de-scanned, before continuing towards the polarizing beam splitter cube. The fraction of returning light that is cross polarized with the incident light is reflected by the polarizing beam splitter cube towards the system's detection arm where it is focused through a slit onto a single channel of a linear detector array. Unlike confocal microscopy which rejects multiply scattered light, LOT relies on scattering to provide depth sensitive measures. Off-axis light emitting from the sample [Fig. 1(b), dashed line] is de-scanned and reflected toward the detector array. However, the off-axis light focuses to a different detector channel whose position is laterally offset from the

#129559 - $15.00 USD Received 4 Jun 2010; revised 28 Aug 2010; accepted 31 Aug 2010; published 2 Sep 2010

on-axis detector channel. The use of a polarizing beam splitter cube is significant because in addition to improving efficiency (compared to a 50:50 beam splitter) the polarizing beam splitter cube acts to suppress specular reflections from the sample surface and from optical components within the system. This is because the polarization state of specularly reflected light remains unchanged, whereas light that has scattered within the tissue will become randomly polarized, such that approximately 50% of this returning light will be reflected by the polarizing beam splitter cube towards the detection arm.

Two recent developments that have expanded the capabilities of LOT are the ability to capture multi-wavelength absorption measurements [12] and the ability to acquire both absorption and fluorescence measurements [18]. To achieve the former, a dispersive element and a 2D PMT array were incorporated such that multi-wavelength light is split into its component wavelengths and imaged onto the face of a 2D PMT array. Each row of the 2D PMT array then acts as a linear detector array, for a specific wavelength of light. Figure 1(c) shows RGB merged LOT 'raw data' images of a phantom consisting of colored absorbers embedded at 3 different depths and simultaneously imaged with 488, 532 and 638 nm light. For fluorescence, a second detection arm is created by placing a multi-line dichroic beam splitter between the galvanometers and the polarizing beam splitter. The multi-line dichroic beam splitter passes the excitation and reflectance/absorption imaging light while reflecting fluorescence light towards a linear array PMT. The use of a multi-line rather than a single edge dichroic beam splitter permits simultaneous fluorescence and multi-wavelength absorption imaging. With these improvements, LOT can acquire 128 x 128 pixel images (source position) with 8 source-detector separations and 3 wavelengths at 20 fps. Decreasing the pixel density to 45 x 45 pixels increases the achievable frame rate to 100 fps.

2.2 Articulating arm

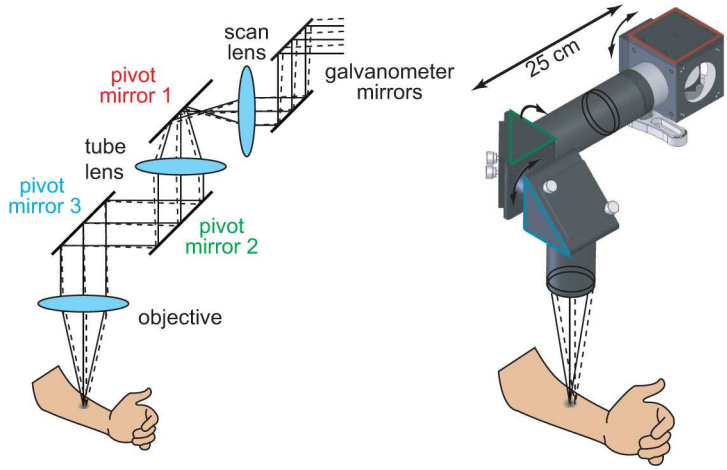

Fig. 2. Schematic drawing of the articulating arm. Pivot mirrors positioned after the scan lens couple the intermediate image plane to the sample plane with three degrees of freedom.

The articulating arm configuration was motivated by the need to image skin lesions situated on areas of the body other than the hands and arms. The articulating arm was implemented by positioning 2" pivot mirrors (BB2-EO2, Thorlabs) distal to the scan lens as shown in Fig. 2. Pivot mirror 1 was mounted in a 2" cube (LC6W, Thorlabs) which was connected to a set of 60mm, SM2 cage plates (LCP01, Thorlabs) via lens tube couplers (SM2T2, Thorlabs) allowing the cube to rotate. Pivot mirrors 2 and 3 were mounted in right angle kinematic cage mounts (KCB2, Thorlabs) which were attached to extension tubes. Rotation by each of the pivot mirrors provided three degrees of freedom.

In order to limit system modifications to components distal to the scan lens, lenses in the articulating arm were selected such that the magnification, and resulting size of the image

#129559 - $15.00 USD Received 4 Jun 2010; revised 28 Aug 2010; accepted 31 Aug 2010; published 2 Sep 2010

formed in the intermediate image plane remained the same. By keeping the magnification unchanged, the source-detector separation distances do not change and modification (as well as associated realignment) of system components proximal to the scan lens is not necessary. The overall length of the articulating arm was limited by the length of the collimated space between lens 1 and the objective. Within this space, the off-axis displacement is translated into an angular deviation which, for longer collimated space lengths, can result in clipping of the transmitted and remitted light. Using longer focal length lenses reduces the angular deviation in the collimated space for a given offset displacement, making them desirable for lens 1 and the objective. However, longer focal length lenses also reduce the system's photon

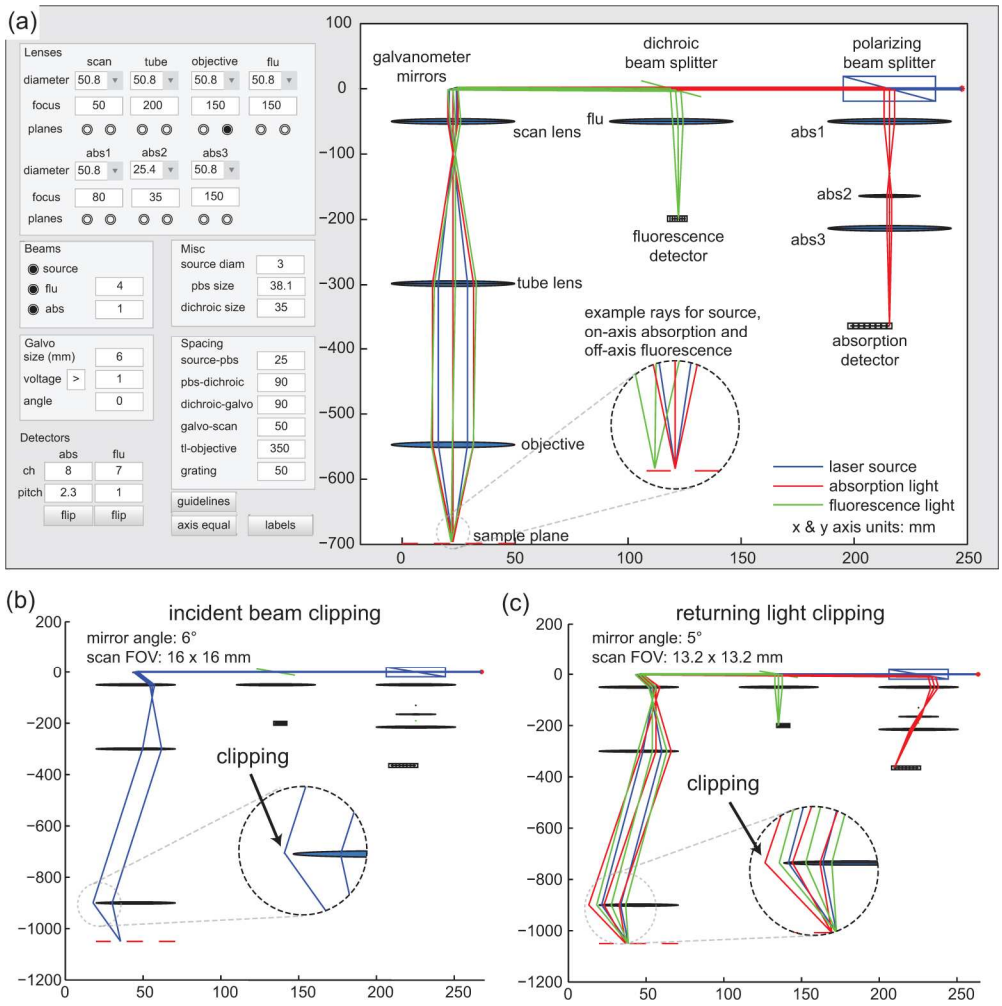

Fig. 3. Screenshots of LOT ray tracing software. (a) Ray tracing for the incident source light (blue), remitted absorption light (red) and emitting fluorescence light (green). All axes are shown in millimeters. (b) Clipping of the incident light is observed when the galvanometer mirrors are rotated during a scan. (c) Clipping of the off-axis returning light during a scan.

migration paths within the tissue. Using larger diameter lenses and mirrors is also beneficial for preventing light clipping. We therefore used 2" diameter lenses and mirrors in the articulating arm.

To optimize the optical paths in the system we developed an LOT ray tracing program using Matlab. The program was implemented using geometric optics and the thin lens equation. The path of each ray is updated each time the user changes a system parameter or

#129559 - $15.00 USD Received 4 Jun 2010; revised 28 Aug 2010; accepted 31 Aug 2010; published 2 Sep 2010

component. The purpose of the program was to verify how and where clipping might occur for different focal length lenses and under various image acquisition settings. A screen shot of the user interface is shown in Fig. 3(a). The user can set the diameter and focal length of all lenses, the sizes of the polarizing beam splitter, dichroic beam splitter, and galvanometer mirrors, the number and pitch of the detector channels, the spacing between components, as well as the angle of the galvanometer mirror. In order to animate a one-dimensional sweep, the program increments the angle of the galvanometer mirror through its minimum and maximum values (as determined by the galvanometer voltage setting) updating the ray position for each galvanometer angle. Figure 3(b) illustrates how the simulation can be used to determine that for this lens configuration, clipping of the incident beam will occur when the galvanometers scan to an angle of 6 degrees, corresponding to a field of view of 16 x 16 mm. Visualizing the returning light path reveals that clipping of the returning beam is more restrictive. Figure 3(c) shows that when the galvanometer mirrors are positioned at an angle of 5 degrees, corresponding to a field of view 13.2 x 13.2 mm, the incident light reaches the sample plane, but clipping of the returning light occurs. In order to scan a 13.2 x 13.2 mm field of view, the distance between the tube lens and objective must be reduced to less than 500 mm.

A valuable feature that we incorporated into the system for clinical studies was a 'field of view indicator'. Since moving the articulating arm causes the field of view to rotate, the LOT control software was modified to trace a bounding box with an attenuated beam, generating a square outline to delineate the region that will be imaged. This region of interest indicator also serves to ensure that no clipping is occurring prior to imaging.

2.3 Fiber bundle

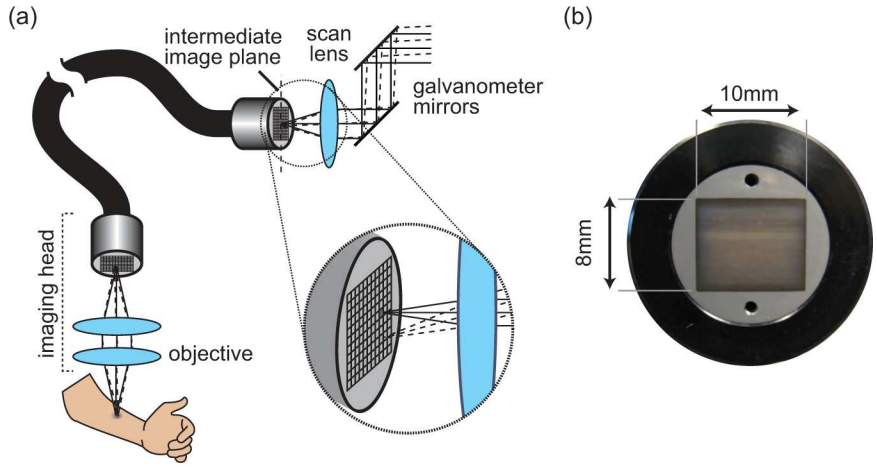

Fig. 4. (a) Schematic diagram of fiber bundle based LOT. (b) Photograph of the fiber bundle end face.

While the articulating arm configuration improved tissue accessibility, we sought to further enhance the flexibility of the patient interface and take a step towards in vivo imaging of internal organs by implementing LOT through a fiber bundle (Fig. 4). The configuration was realized by placing a 4 ft imaging fiber bundle (IG-163, Schott) in the intermediate image plane formed by the scan lens. The 8 mm x 10 mm format bundle, with individual core spacing of 10 μm, couples the intermediate image plane to a position closer to the sample plane. An objective lens positioned at the distal end of the fiber (nearest the sample plane) focuses light to and from the sample. As the galvanometers scan the incident light over the proximal face of the fiber bundle, light is selectively transmitted down different fibers forming a moving source on the distal fiber face. The imaging head effectively images the moving source onto the surface of the sample while also imaging light emerging from the

#129559 - $15.00 USD Received 4 Jun 2010; revised 28 Aug 2010; accepted 31 Aug 2010; published 2 Sep 2010

sample back onto the distal face of the fiber bundle. The fiber bundle transmits this returning light to the scan lens intermediate image plane where it emerges and continues along the light detection path.

As with the articulating arm implementation, system modifications were limited to components distal to the scan lens. The lenses used in the imaging head were selected to keep the image size in the scan lens intermediate image plane the same, however since light clipping is not as problematic as with the articulating arm, smaller diameter and shorter focal length lenses were used in the imaging head, allowing it to be more compact. The higher numerical aperture of the shorter focal length lenses also permits higher light collection efficiency by the imaging head.

Implementation of the fiber bundle system was confounded by 3 issues: loss of polarization in the fiber bundle, specular reflections from the proximal and distal ends of the fiber bundle and, light losses due the fiber bundles packing fraction.

The fiber bundle affects polarization control because light entering each fiber of the bundle loses its polarization over the course of its journey to the distal end. If this light is then specularly reflected from the sample, or from the lenses in the imaging head, it can no longer be distinguished from multiply scattered light when it returns through the fiber bundle.

Reflections from the faces of the fiber bundle were also a significant obstacle, exacerbated by the polished 90° ends of the particular bundle used in our implementation. In spite of the 500:1 extinction ratio of our polarizing beam splitter cube, in some cases this reflection was large enough to saturate our detector, leading us to suspect that some contribution to the reflection was also originating from the inner surface of the distal end of the bundle. We found that this effect could be somewhat reduced by advancing the face of the fiber bundle just past the intermediate image plane such that scanning beam is focused just beyond the fiber bundle face rather than at the surface. However, this reduces the coupling efficiency of the bundle and increases the spot size of the scanning beam at the sample.

A final challenge associated with the fiber bundle configuration was light loss due to the bundle's packing fraction [19]. The cladding of each individual fiber, as well as the interfiber space does not carry light, thereby lowering the throughput of the fiber. At 532 nm we measured the light loss for one pass of the bundle to be 40%, which includes losses due to both the packing fraction and reflection off the fiber bundle face.

Having modified our basic LOT system to incorporate either the articulating arm or the fiber bundle, we then sought to characterize the performance of each configuration using tissue-like phantoms as described below.

3. Phantom imaging

3.1 Phantom geometry

A phantom consisting of human hair embedded in an absorbing and scattering background medium was used to compare the imaging performance of our two configurations. The tissue-like phantom consisted of an agarose based hydrogel (A9539, Sigma) with intralipid (I141, Sigma) and instant coffee (Medaglia D'Oro) added to provide reduced scattering and absorption coefficients at 532 nm of 1 mm^{-1} and 0.2 mm^{-1} respectively. These values were chosen to mimic the optical properties of rodent brain.

The agarose solution was prepared as described in [20], replacing ink with instant coffee as the absorber. Once mixed, most of the liquid solution was poured into a mold to set while the remainder was used to make a 200 μm thick sheet by sandwiching the gel between two microscope slides with a spacer [21]. When the gels hardened (~10 minutes), the phantom was assembled by placing a piece of hair on the surface of the molded gel and then covering the hair with the thin gel sheet effectively embedding the hair at a depth of 200 μm. Figure 5 shows a schematic cross-section and photograph of the phantom.

#129559 - $15.00 USD Received 4 Jun 2010; revised 28 Aug 2010; accepted 31 Aug 2010; published 2 Sep 2010

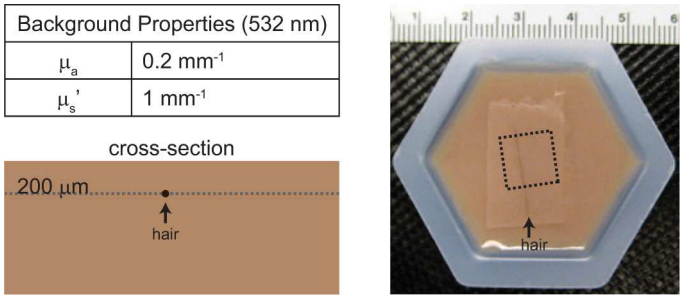

Fig. 5. Imaging phantom: schematic drawing and photograph. Arrowheads indicate location of hair in each. Dashed line in the photograph shows the LOT imaging region of interest.

3.2 Imaging

The phantom was imaged using 532 nm light with both the articulating arm and fiber bundle configurations. The intensity of the incident light at the sample plane was 1 mW which, for the fiber bundle configuration, required increasing the intensity of light entering the fiber bundle to offset transmission loses. Scanning was performed with 300 x 300 source positions (pixels) and 8 source-detector separations (300 μm offset increments). A total of 100 frames were acquired at a frame rate of 1.1 fps. In a typical LOT imaging session fewer frames are acquired (~15-20) during a scan, and at higher frame rates to reduce motion artifacts. Here we acquired more frames for statistical analysis. To reduce the possibility of motion artifacts, the articulating arm (or fiber bundle) was positioned over the phantom and immobilized for the duration of the scan. Since the intensity of light detected by the wider off-axis detector channels of our PMT is much lower than that detected by the narrow detector channels, we placed a thin attenuating transparency film in front of the first 3 channels of the PMT. This allowed us to increase the high voltage applied to the PMT to improve the low level light detection of the off-axis channels without saturating the first few channels. The dashed lines in Fig. 5 indicate the 10 mm x 10 mm scan region of interest. A slightly smaller region of interest was scanned with the fiber bundle because of the 8 x 10 mm area of the fiber bundle face (since the imaging head is currently implemented with 1x magnification). 'Dark scans' were acquired to allow correction for specular reflections and were identical to the normal scans except that no object was placed in the sample plane.

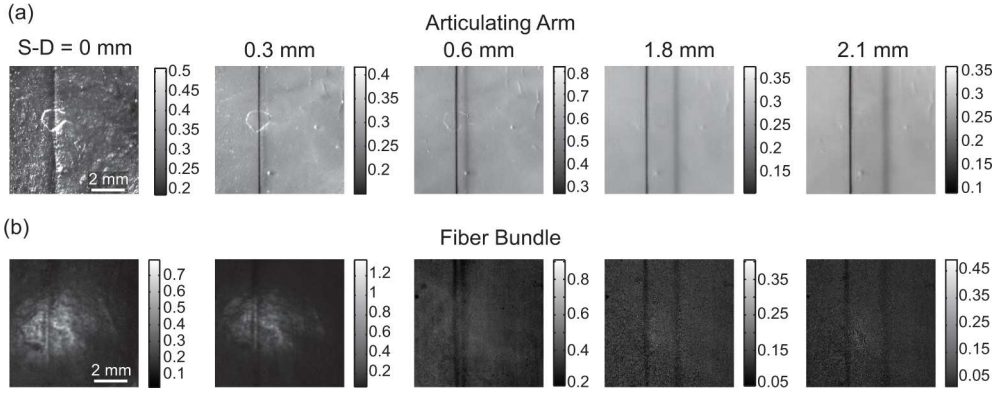

Fig. 6. LOT 'raw data' images after dark subtraction. (a) Articulating arm. (b) Fiber bundle. Color bars are in units of volts.

Figure 6 shows LOT 'raw data' images of the hair phantom obtained using the (a) articulating arm and (b) fiber bundle (both after dark subtraction). In the narrowest source-detector separation (0 mm), the hair appears as a single vertical line. A shadow appears alongside the hair in the off-axis source-detector image which is characteristic of LOT data

#129559 - $15.00 USD Received 4 Jun 2010; revised 28 Aug 2010; accepted 31 Aug 2010; published 2 Sep 2010

sets [22]. The offset distance of the shadow is indicative of the effective source-detector separation since the shadow occurs when the source is positioned adjacent to the hair, but the detector is positioned over the hair. The narrowest source-detector separation (equivalent to confocal) accentuates the rough surface of the phantom).

3.3 Noise model and comparison of contrast and noise levels

The detected signals from our LOT system can be expressed as:

$$M_{s,d} = g_d \left(S_{s,d} + D_{s,d} + O_d \right) \tag{1}$$

where $M_{s,d}$ is the measurement from source position s and detector d, $S_{s,d}$ is the signal contribution from the sample, $D_{s,d}$ is the signal contributed by reflections from intermediate optics, O_d is the signal offset from the detector dark current, and g_d is the gain of detector d and its associated transimpedance amplifier circuit [18]. A 'dark scan' would therefore be given by g_d ($D_{s,d}$ + O_d), and so after dark subtraction, Eq. (1) reduces to:

$$M_{s,d} = g_d \left(S_{s,d} + D_{s,d} + O_d \right) - g_d \left(D_{s,d} + O_d \right) = g_d S_{s,d} \tag{2}$$

In order to evaluate contrast, we must first define our background. In our hair phantom, the background corresponds to the homogenous regions surrounding the hair. Background signal for a single source-detector separation was calculated by first averaging the data across frames as illustrated in Fig. 7(a). With the hair running vertically down the resulting image, the data was averaged down each column creating a profile (S_{avg}) with an almost uniform background level and a dip occurring at the position of the hair. The average background ($S_{avgBkgd}$) was calculated from this background level and the percent change (%Δ) in terms of our noise model calculated by:

$$\%\Delta = \frac{\left(g_d S_{avgBkgd} - g_d S_{avg} \right)}{g_d S_{avgBkgd}} \times 100 = \frac{\left(S_{avgBkgd} - S_{avg} \right)}{S_{avgBkgd}} \times 100 = 1 - \frac{S_{avg}}{S_{avgBkgd}} \times 100 \tag{3}$$

The percent changes in signal for select source-detector separations are shown in Fig. 7(b). It is important to note the differences between the plots for the articulating arm and the fiber bundle. The two peaks, corresponding to the presence of the hair in the data, are quite different in peak amplitude for the articulating arm, whereas the two peaks have similar sizes for the fiber bundle. The first peak (to the left in each plot) corresponds to the signal change when the source beam scans over the hair, whereas the second peak (to the right) corresponds to when the detector is effectively scanned over the hair. For the articulating arm, the size of the scanning source beam is diffraction-limited, leading to a high and narrow point spread function, whereas the effective detector size is approximately 300 microns wide, leading to a lower and wider second peak. The fiber bundle cross-sections illustrate that the fiber bundle causes the size of the scanning beam to increase at the sample plane, leading to a lower and wider first peak. Therefore, in order to objectively compare contrast between the two configurations, we compare the amplitude of the second peak (detector shadow) rather than the first peak. Absorption contrast, as shown in Fig. 7(c) (left), is given by the maximum percent change in the hair shadow signal from the baseline for both configurations.

As expected, the contrast for both configurations is similar. The shape of the contrast as a function of source-detector separation can be explained as follows: For the narrower source-detector separation distance, contrast is lower, since light detected by the narrower source-detector separations has mostly probed superficial regions above the hair. Contrast increases for the wider source-detector separations since this light has probed deeply enough to interact with the hair, although contrast decreases again when source-detector separations are wide enough to be more sensitive to regions that are deeper than the hair. The slight differences between the contrast profiles for the two configurations may be attributable to the slightly different effective source-detector separations and numerical apertures of the two

#129559 - $15.00 USD Received 4 Jun 2010; revised 28 Aug 2010; accepted 31 Aug 2010; published 2 Sep 2010

measurement geometries and therefore the different relative depth sensitivities of each measurement.

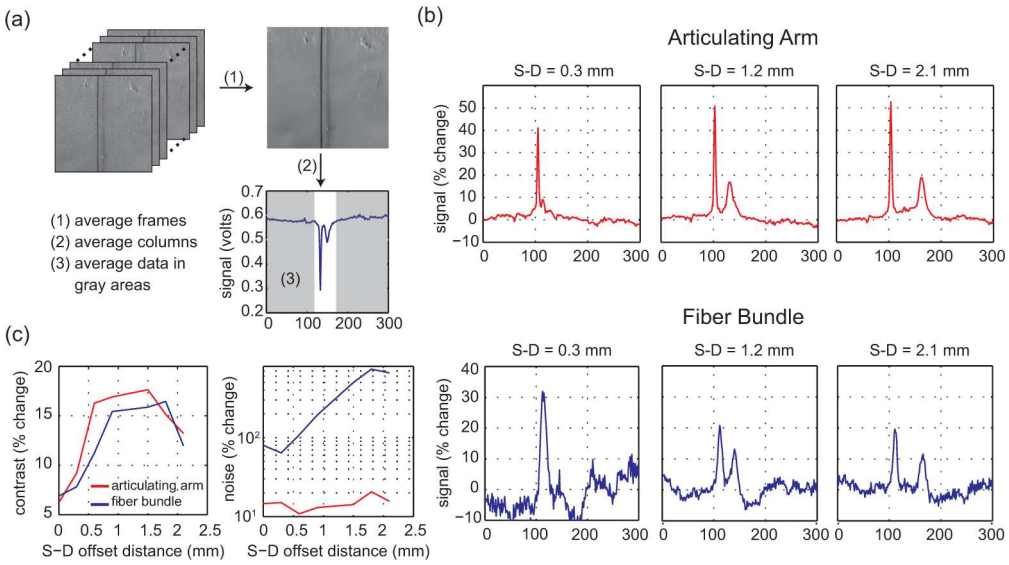

Fig. 7. (a) Background signal was calculated from the average of 100 frames (1). The averaged frame was then averaged down columns creating a profile of the frame (2). Background regions were selected and averaged from the profile (3). (b) The percent change from the background signal provided a measure of contrast. Plots show the percent change for the articulating arm (top) and fiber bundle (bottom) at three source-detector (S-D) separation distances. (c) Contrast and noise plots for each configuration.

The challenges associated with the current fiber bundle implementation are evident in the noise plots shown in Fig. 7(c). Image noise was evaluated by first calculating each pixel's percent change across all 100 repeated images. The standard deviation of each pixel's percent change was then calculated and averaged for all pixels in the image resulting in a measure of noise. While noise for the articulating arm implementation showed little change across source-detector separation distances, the noise for the fiber bundle implementation increased substantially as the source-detector separation distance increased.

The higher noise levels in the fiber bundle images (compared to the articulating arm) can be attributed to the large specular reflections from the faces of the fiber bundle. The contrast values shown in Fig. 7(b) are relatively unaffected by this confound, since our calibration scheme includes subtraction of a 'dark scan' corresponding to the case when no object is present. However, by comparing the amplitude of the 'dark scan' signal for the fiber bundle to measured data with an object present, we were able to deduce that 50-80% of our measured signal was due to light reflecting from the faces of the fiber bundle. Furthermore, inspection of 100 repeated scans of the fiber bundle's dark signal revealed significant, structured variance that we hypothesize is due to small fluctuations in the relative position of each fiber with respect to the laser beam scanning the bundle's face. This overwhelming variance is then superimposed onto the small signal that actually traversed the fiber bundle and visited the sample. Since the signal from the phantom becomes weaker as the source-detector separation distance increases, the noise from these reflections becomes more prominent in the wider source-detector separation distance images. Shot noise is an additional confound that may become problematic in this case because its magnitude increases as the square root of light intensity. Typically an increase in noise is offset by an increase in the average signal. However, in our case, the intensity of the proximal reflection signal only increases the noise level, but not the signal.

We expect that reduction of reflections from the fiber bundle's ends will significantly improve the relative performance of the fiber bundle configuration. A first step would be to

#129559 - $15.00 USD Received 4 Jun 2010; revised 28 Aug 2010; accepted 31 Aug 2010; published 2 Sep 2010

obtain an imaging fiber bundle whose ends have been polished to an angle other than 90°, although other groups have addressed similar specular reflections at the fiber bundle face by using an index-matching oil at the fiber face [23] and tilting the fiber bundle [24]. The use of a higher extinction ratio polarizing beam splitter cube would also aid in rejecting specular reflections from the proximal face. Future endoscopic embodiments of LOT could also be implemented with distal scanning optics (e.g. using MEMs), or even high-density solid-state arrays of light sources and detectors.

4. Conclusion

We have developed and demonstrated acquisition of LOT data through both an articulating arm and a fiber optic bundle. Of the two configurations, the images acquired through the articulating arm had a higher contrast, lower noise levels and reduced specular reflections compared to those obtained with the fiber bundle. However, the fiber bundle provided usable data that offered significantly more flexible image acquisition and much improved potential for imaging of internal organs. The systems described here improve tissue accessibility and are sufficient for clinical skin imaging. However, further miniaturization is necessary to facilitate LOT imaging of internal epithelial tissues such as the colon, esophagus, oral mucosa, and cervix where we believe LOT imaging will be useful for identifying and monitoring pathologies.

Acknowledgments

This research was supported in part by the National Institutes of Health (R21NS053684, R01NS063226, and U54CA126513) and the Wallace H. Coulter Foundation. B. Chen receives National Science Foundation graduate fellowship funding.

#129559 - $15.00 USD Received 4 Jun 2010; revised 28 Aug 2010; accepted 31 Aug 2010; published 2 Sep 2010